GEOPHYSICS, VOL. 91, NO. 1 (JANUARY-FEBRUARY 2026); P. WA47–WA56, 9 FIGS., 1 TABLE.
10.1190/GEO2025-0022.1

Wave simulation in two-temperature thermoporoelastic media with dual-phase-lag heat conduction

Yunfei Liu[1], Li-Yun Fu[2], José M. Carcione[3], Wubing Deng[2], and Wanting Hou[4]

ABSTRACT

We develop a two-temperature dual-phase-lag (TT-DPL) thermoporoelasticity theory that extends the classical single-temperature theory. The theory distinguishes between solid and fluid temperatures and includes fluid-solid coupling terms related to temperature-displacement and temperature-conductivity coefficients, which describe the interactions and heat conduction between the skeleton and pore fluids. A plane-wave analysis predicts five waves, namely, a fast P, slow P, fast thermal (T1), slow thermal (T2), and an S wave. The results indicate that the slow P and slow T are mainly influenced by the pore fluid, whereas the fast P and fast T are mainly influenced by the solid phase. The TT-DPL model leads to more velocity dispersion and thermal attenuation, particularly at high frequencies. A rotated, staggered-grid finite-difference method, combined with an effective absorbing boundary, is used to compute wavefield snapshots. The type of fluid in the rock affects the T-wave behavior, with the fluid's viscosity playing an important role.

INTRODUCTION

The theory of temperature-dependent wave propagation in fluid-saturated porous rocks is relevant in many geophysical applications, such as geothermal exploration, thermally enhanced oil recovery, and ultradeep hydrocarbon exploration (Jacquey et al., 2015; Fu, 2017, 2019; Poletto et al., 2018; Li et al., 2023; Cheng et al., 2024), wherein the skeleton and pore fluids exhibit large differences in temperature and thermal properties. Such media involve complex thermomechanical coupling processes (Breede et al., 2013; Cui and Wong, 2021; Jian et al., 2022; Wang et al., 2023), including interactions within each phase and interphase coupling caused by heat transfer proportional to the temperature difference between the phases. The resulting coupling effects significantly affect wave dissipation and attenuation (Treitel, 1959; Savage, 1966; Armstrong, 1984). In this study, the problem is investigated through analytical methods and numerical simulations.

The theory of thermoporoelasticity (Noda, 1990; Nield and Bejan, 2006; Sharma, 2008) combines the heat equation and Biot's equations of poroelasticity to describe the coupling between the displacement and temperature fields. The numerical simulations (Carcione et al., 2019) and Green function solvers (Wei et al., 2020) show the effect of fluid viscosity and thermal properties on wave attenuation. The theory has been expanded to include double porosity (pores and cracks) (Kumar et al., 2017; Li et al., 2021; Kumar et al., 2023) and thermoacoustoelasticity for wave propagation in preheated and prestressed rocks (Yang et al., 2025). In particular, Li et al. (2023) apply the double-porosity thermoporoelasticity theory to develop a coupled thermo-hydro-mechanical model for cyclic recovery in fractured-vuggy reservoirs. Reflection and transmission (R/T) of inhomogeneous body waves were obtained (Wang et al., 2021; Kumar et al., 2022; Liu et al., 2022; Hou et al., 2023) and applied to Olkaria geothermal reservoirs for time-lapse reflection seismic monitoring (Cheng et al., 2024). However, these formulations are based on a single-temperature (ST) and a single-phase-lag (SPL) relaxation time of heat conduction (Lord and Shulman, 1967), assuming only an average temperature over the porous rock and inadequately describing the thermal-mechanical coupling caused by heat transfer between the solid and fluid phases.

A second generalization of Biot theory is known as ST thermoporoelasticity theory with a dual-phase-lag (DPL) relaxation time of heat conduction, which has been proposed for metals (Tzou, 1995a) and, recently, for wave propagation in fluid-saturated porous rocks

Manuscript received by the Editor 24 January 2025; revised manuscript received 27 May 2025; published ahead of production 8 August 2025; published online 26 November 2025.
[1]China University of Petroleum (East China), State Key Laboratory of Deep Oil and Gas, Qingdao, China. E-mail: 18382268254@139.com.
[2]China University of Petroleum (East China), State Key Laboratory of Deep Oil and Gas, Qingdao, China and Qingdao Marine Science and Technology Center, Laboratory for Marine Mineral Resources, Qingdao, China. E-mail: lfu@upc.edu.cn (corresponding author); wubing.deng@foxmail.com.
[3]National Institute of Oceanography and Applied Geophysics — INOGS, Trieste, Italy. E-mail: jose.carcione@gmail.com.
[4]Chengdu University of Technology, School of Geophysics, Chengdu, China. E-mail: hwtupc@163.com.

(Liu et al., 2023; Kumar et al., 2024). The ST-DPL thermoporoelastic model involves two lag times, one of which is used in a way similar to the SPL term to describe the macroscopic heat flux relaxation of the rock skeleton, and the other is introduced for the temperature gradient relaxation that characterizes the fluid phase. However, the ST-DPL theory neglects the thermal coupling between the solid and fluid caused by heat transfer between the phases. It only considers small relaxation times caused by very small differences in the thermal properties of the solid frame and the pore filling. It fits the properties of metals with delay times well on the order of picoseconds (Tzou, 1995b) and those of biological materials on the order of microseconds (Xu et al., 2008; Abd-Alla et al., 2020). However, as demonstrated by some experiments (Kaminski, 1990; Vedavarz et al., 1992; Mitra et al., 1995), the relaxation times of the skeleton and pore fluids vary widely, ranging from seconds to mere fractions of minutes. Compared to the solid, the fluid is more sensitive to temperature, exhibiting larger relaxation effects on wave attenuation (Batzle and Wang, 1992; Schmitt, 1999; Han et al., 2008; Rabbani and Schmitt, 2018; Yuan et al., 2019). Youssef (2007) extends the ST-SPL thermoporoelastic theory by considering the differences in temperature and relaxation time between the solid and the fluid. The resulting two-temperature (TT) theory with DPL heat conduction accounts for thermal-mechanical coupling caused by interphase heat transfer, predicting an additional slow thermal wave (T2) (Singh, 2011). In addition to the usual coefficients of thermal expansion of single-phase media, there are two coupling coefficients. Hou et al. (2024) obtain the R/T of inhomogeneous body waves at the interface between two TT-DPL media. However, these theoretical studies lack numerical simulations to illustrate the effects of thermal properties on wave dissipation. In this study, this problem is addressed using a finite-difference (FD) method with rotated staggered grids.

Seismic-wave simulations in thermoporoelastic (nonisothermal) models are relevant for ultradeep geophysical exploration. Several techniques have been developed for use in isothermal media, such as the FD (Zhang et al., 2014) method, the finite element method (Serón et al., 1990), the boundary element method (Fu and Mou, 1994; Hu et al., 2009), and the spectral method (Faccioli et al., 1997). Notably, simulations have been conducted to investigate the thermoelasticity effects related to wave attenuation and velocity dispersion using staggered FD grids (Veres et al., 2013; Hou et al., 2021a) and the Fourier pseudospectral method (Carcione et al., 2018, 2019). Although staggered grids improve the FD method's accuracy, they are prone to instability and boundary artifacts. To address these problems, rotating staggered grids (RSGs) and nonsplit convolutional perfectly matched layer methods have been developed to mitigate instability, eliminate spurious modes, and reduce low-frequency energy reflections (Komatitsch and Martin, 2007; Wang et al., 2019).

In this study, we first derive Youssef's TT-DPL equations. The analysis with homogeneous plane waves predicts the existence of four P waves (the fast P, slow P, fast T, and slow T) and one S wave. Variations in the thermal properties of solids and fluids, along with differences in thermal diffusion mechanisms within the medium, lead to increased velocity dispersion and attenuation. The slow P wave is associated with pressure differences, whereas the slow T wave is more influenced by the fluid phase. We then model the wavefields by solving the governing equations using the FD method and analyze the physics of wave propagation. The simulations can be used for the inversion of seismic thermoelastic properties and fluid parameters in high-temperature, high-pressure reservoirs.

TT-DPL THERMOPOROELASTICITY THEORY

Heat conduction

In the ST-SPL theory, the relaxation time τ is introduced to overcome the unphysical results that arise from the classical Fourier heat conduction equation:

$$\gamma \Delta T = \left(\frac{\partial}{\partial t} + \tau \frac{\partial^2}{\partial t^2}\right)[CT + \beta T_0(e_{kk} + e_f)], \tag{1}$$

where γ is the bulk heat conduction coefficient (or thermal conductivity); C is the bulk specific heat per unit volume in the absence of deformation; β is the coefficient of thermal stress; T is the temperature increment relative to a reference temperature T_0; e_{kk} and e_f are the solid and fluid strains, respectively; Δ is the Laplacian operator; and a dot above a variable indicates the time differentiation.

The inherent thermal properties of the medium, such as τ, γ, β, and C, are considered equivalent parameters in the theory, assuming that there is no difference between the two phases. However, studies have shown that the thermal relaxation times of the solid and fluid phases can differ by several orders of magnitude at room temperature (Kjartansson, 1979). Following the approach of Youssef (2007), we treat the heat conduction in those phases separately. In this formulation, coupling coefficients between the solid and fluid phases are introduced. The TT-DPL equations are

$$\begin{cases} \gamma_s' \Delta T_s = \Gamma_{1s}^2 (F_{11} T_s + F_{12} T_f) + [T_0 \Gamma_{2s}^2 (R_{11} e_{kk} + R_{21} e_f)] \\ \gamma_f' \Delta T_f = \Gamma_{1f}^2 (F_{21} T_s + F_{22} T_f) + [T_0 \Gamma_{2f}^2 (R_{12} e_{kk} + R_{22} e_f)] \end{cases}, \tag{2}$$

where

$$\begin{cases} \gamma_s' = (1-\phi)\gamma_s, \gamma_f' = \phi\gamma_f \\ R_{11} = (1-\phi)\beta_s, R_{22} = 3M\phi\alpha_f \\ R_{12} = \alpha\beta_f, R_{21} = 3M(\alpha-\phi)(1-\phi)\alpha_s \\ J = 3\alpha_s R_{12} + \alpha_{fs} R_{22} \\ F_{11} = (1-\phi)C_s, F_{22} = \phi C_f \rho_f \\ F_{12} = F_{21} = -JT_0 \\ \Gamma_{mn}^2 = \partial_t + \tau_{mn}\partial_{tt}, m = 1,2, n = s,f \end{cases}, \tag{3}$$

where the subscripts "s" and "f" denote the solid and fluid phases, respectively; ρ is the density; ϕ is the porosity; α_{fs} is the coupling between the phases; and R, F, and J are the mixed and thermal coefficients (Pecker and Deresiewicz, 1973; Youssef, 2007; Carcione et al., 2019).

Governing equations

In the absence of elastic and heat sources, the constitutive relations for stress-strain are (Youssef, 2006, 2007; Carcione et al., 2019)

$$\begin{cases} \sigma_{ij} = 2\mu e_{ij} + [\lambda e_{kk} + \alpha M(\alpha e_{kk} + e_f) - R_{11} T_s - R_{12} T_f]\delta_{ij} \\ \sigma_f = \phi M(\alpha e_{kk} + e_f) - R_{21} T_s - R_{22} T_f \end{cases}, \tag{4}$$

where σ_{ij} and σ_f are the stress components of the rock skeleton and fluid, respectively; λ and μ are the dry-rock Láme constants; δ_{ij} is the Kronecker delta; and u_i and w_i ($i = x, y, z$) are the displacement components of the skeleton (or frame) and fluid (relative to the skeleton), respectively.

Biot's coefficients are

$$\begin{cases} \alpha = 1 - \frac{K_m}{K_s}, K_m = \lambda + \frac{2}{3}\mu \\ M = \left(\frac{\alpha-\phi}{K_s} + \frac{\phi}{K_f}\right)^{-1} \end{cases}, \tag{5}$$

where K_s and K_f are the bulk moduli of the solid and fluid, respectively.

The dynamic equations are

$$\begin{cases} \sigma_{ij,j} = \rho\ddot{u}_i + \rho_f\ddot{w}_i \\ (-p)_{,i} = \rho_f\ddot{u}_i + m\ddot{w}_i + r\dot{w}_i \end{cases}, \tag{6}$$

with

$$\begin{cases} \rho = (1-\phi)\rho_s + \phi\rho_f \\ m = \frac{\varsigma\rho_f}{\phi}, r = \frac{\eta}{\kappa} \end{cases}, \tag{7}$$

where p is the fluid pressure, ρ is the bulk density, ς is the tortuosity, η is the fluid viscosity, and κ is the permeability of the frame.

Substituting the stress-strain relations in equation 4 into the dynamical equation 6, we obtain the following compact equations that describe the coupling between the displacement components and temperature fluctuations:

$$\begin{cases} (\lambda+\mu+\alpha^2 M)u_{j,ij} + \mu u_{i,jj} + \alpha M w_{j,ij} - R_{11}T_{s,i} - R_{12}T_{f,i} = \rho\ddot{u}_i + \rho_f\ddot{w}_i \\ M(\alpha u_{j,ij} + w_{j,ij}) - R_{21}T_{s,i} - R_{22}T_{f,i} = \rho_f\ddot{u}_i + m\ddot{w}_i + r\dot{w}_i \\ \gamma_s' T_{s,ii} = \Gamma_{1s}^2(F_{11}T_s + F_{12}T_f) + [T_0\Gamma_{2s}^2(R_{11}u_{i,i} + R_{21}w_{i,i})] \\ \gamma_f' T_{f,ii} = \Gamma_{1f}^2(F_{21}T_s + F_{22}T_f) + [T_0\Gamma_{2f}^2(R_{12}u_{i,i} + R_{22}w_{i,i})] \end{cases}. \tag{8}$$

We observe that the coupling between heat and strain involves only volume strains, as indicated by the dynamic equation 6. The displacement-temperature interaction is governed by a single mechanism: the expansion and contraction propagation of P waves induces a dissipative decaying T-wave mode. This mechanism is experimentally confirmed as a heat-wave interaction. The TT-SPL model is derived with $\tau_{1n} = \tau_{2n}$ ($n = s$ or f), whereas the generalized case (TT-DPL) considers $\tau_{1n} \neq \tau_{2n}$. A plane-wave analysis for determining the phase velocity and attenuation factor of the wave modes is shown in Appendix A.

PARTICLE VELOCITY-STRESS-TEMPERATURE FORMULATION

We consider the (x,z)-plane and solve the differential equations using a first-order time-stepping approach known as the particle velocity-stress formulation. The equations are reformulated into new expressions suitable for numerical simulations. Equation 4 becomes

$$\begin{cases} \dot{v}_x = \beta_{11}(\partial_x\sigma_{xx} + \partial_z\sigma_{xz} - f_x) - \beta_{12}(\partial_x p + rq_x) \equiv \Pi_x \\ \dot{v}_z = \beta_{11}(\partial_x\sigma_{xz} + \partial_z\sigma_{zz} - f_z) - \beta_{12}(\partial_z p + rq_z) \equiv \Pi_z \\ \dot{q}_x = \beta_{21}(\partial_x\sigma_{xx} + \partial_z\sigma_{xz} - f_x) - \beta_{22}(\partial_x p + rq_x) \equiv \Omega_x \\ \dot{q}_z = \beta_{21}(\partial_x\sigma_{xz} + \partial_z\sigma_{zz} - f_z) - \beta_{22}(\partial_z p + rq_z) \equiv \Omega_z \\ \dot{\sigma}_{xx} = (\lambda+2\mu)\partial_x v_x + \lambda\partial_z v_z + \alpha^2 M(\partial_x v_x + \partial_z v_z) + \alpha M(\partial_x q_x + \partial_z q_z) - R_{11}\psi_s - R_{12}\psi_f \\ \dot{\sigma}_{zz} = (\lambda+2\mu)\partial_z v_z + \lambda\partial_x v_x + \alpha^2 M(\partial_x v_x + \partial_z v_z) + \alpha M(\partial_x q_x + \partial_z q_z) - R_{11}\psi_s - R_{12}\psi_f \\ \dot{\sigma}_{xz} = \mu(\partial_x v_x + \partial_z v_z) \\ \dot{p} = -\alpha M(\partial_x v_x + \partial_z v_z) - M(\partial_x q_x + \partial_z q_z) + R_{21}\psi_s + R_{22}\psi_f \\ \dot{T}_s = \psi_s \\ \dot{T}_f = \psi_f \\ \dot{\psi}_s = A_0 \times \begin{Bmatrix} F_{12}\tau_s\left[\gamma_f(\partial_{xx}\psi_f + \partial_{zz}\psi_f) - F_{21}\psi_s - F_{22}\psi_f - T_0\begin{pmatrix} R_{12}(\partial_x v_x + \partial_z v_z + \tau_f(\partial_x\Pi_x + \partial_z\Pi_z)) \\ +R_{22}(\partial_x q_x + \partial_z q_z + \tau_f(\partial_x\Omega_x + \partial_z\Omega_z)) \end{pmatrix}\right] \\ -F_{22}\tau_f\left[\gamma_s(\partial_{xx}\psi_s + \partial_{zz}\psi_s) - F_{11}\psi_s - F_{12}\psi_f - T_0\begin{pmatrix} R_{11}(\partial_x v_x + \partial_z v_z + \tau_s(\partial_x\Pi_x + \partial_z\Pi_z)) \\ +R_{21}(\partial_x q_x + \partial_z q_z + \tau_s(\partial_x\Omega_x + \partial_z\Omega_z)) \end{pmatrix}\right] \end{Bmatrix} \\ \dot{\psi}_f = A_0 \times \begin{Bmatrix} -F_{11}\tau_s\left[\gamma_f(\partial_{xx}\psi_f + \partial_{zz}\psi_f) - F_{21}\psi_s - F_{22}\psi_f - T_0\begin{pmatrix} R_{12}(\partial_x v_x + \partial_z v_z + \tau_f(\partial_x\Pi_x + \partial_z\Pi_z)) \\ +R_{22}(\partial_x q_x + \partial_z q_z + \tau_f(\partial_x\Omega_x + \partial_z\Omega_z)) \end{pmatrix}\right] \\ +F_{21}\tau_f\left[\gamma_s(\partial_{xx}\psi_s + \partial_{zz}\psi_s) - F_{11}\psi_s - F_{12}\psi_f - T_0\begin{pmatrix} R_{11}(\partial_x v_x + \partial_z v_z + \tau_s(\partial_x\Pi_x + \partial_z\Pi_z)) \\ +R_{21}(\partial_x q_x + \partial_z q_z + \tau_s(\partial_x\Omega_x + \partial_z\Omega_z)) \end{pmatrix}\right] \end{Bmatrix} \end{cases}, \tag{9}$$

with

$$\begin{cases} \begin{bmatrix} \beta_{11} & \beta_{12} \\ \beta_{21} & \beta_{22} \end{bmatrix} = (\rho_f^2 - \rho m)^{-1}\begin{bmatrix} -m & \rho_f \\ \rho_f & -\rho \end{bmatrix} \\ A_0 = \frac{1}{\tau_s\tau_f(F_{12}F_{21} - F_{11}F_{22})} \end{cases}, \tag{10}$$

where v_i and q_i are the components of the particle velocity fields of the frame and fluid relative to the frame, respectively.

Equation 9 can be expressed in matrix form as

$$\dot{\mathbf{v}} + \mathbf{s} = \mathbf{M}\mathbf{v}, \tag{11}$$

where

$$\mathbf{v} = [v_x, v_z, q_x, q_z, \sigma_{xx}, \sigma_{zz}, \sigma_{xz}, p, T_s, T_f, \psi_s, \psi_f]^{\mathrm{T}} \tag{12}$$

is the unknown vector, and $\mathbf{s}$ is the source vector. Matrix $\mathbf{M}$ is the propagation operator derived from equations 9 and 10. The solution to equation 11, subject to the initial condition $\mathbf{v}(0) = \mathbf{v}_0$, is formally given by

$$\mathbf{v}(t) = \exp(t\mathbf{M})\mathbf{v}_0 + \int_0^t \exp(\tau\mathbf{M})\mathbf{s}(t-\tau)d\tau, \tag{13}$$

where $\exp(t\mathbf{M})$ is called the evolution operator.

The eigenvalues of $\mathbf{M}$ may have negative real parts and differ greatly in magnitude. The presence of large and small eigenvalues indicates that the problem is stiff. Moreover, the presence of real positive eigenvalues can induce instability in the time-stepping method. To address these issues, the differential equations are solved using the splitting algorithm proposed by Carcione and Quiroga-Goode (1995) and Carcione and Seriani (2001). The propagation matrix can be partitioned as

$$\mathbf{M} = \mathbf{M}_{r'} + \mathbf{M}_{s'}, \tag{14}$$

where the subscript r' indicates the regular matrix and the subscript s' denotes the stiff matrix, involving the coupling terms. The evolution operator can be expressed as $\exp(\mathbf{M}_{r'} + \mathbf{M}_{s'})t$. It is easy to show that

$$\exp(\mathbf{M}dt) = \exp\left(\frac{1}{2}\mathbf{M}_{s'}dt\right)\exp(\mathbf{M}_{r'}dt)\exp\left(\frac{1}{2}\mathbf{M}_{s'}dt\right), \tag{15}$$

has the second-order accuracy $O(dt^2)$. We solve the equations using the time integration method described in Appendix B.

PHYSICS AND SIMULATIONS

The properties of water-/oil-/gas-saturated rock are provided in Table 1, and the values are determined by Kjartansson (1979), Singh (2011), Carcione (2022), and Hou et al. (2023). It is worth noting that the relaxation time is challenging to determine experimentally, particularly in porous rocks. We can calculate using the method outlined in Section 5.2 of Liu et al (2023). Figure 1 shows the combined effects of water-saturated models on frequency-dependent velocities and the attenuation factors of P waves. The TT-DPL model assumes $\tau_{1n} \neq \tau_{2n}$ ($n = s, f$), whereas $\tau_{1n} = \tau_{2n}$ in the TT-SPL model.

Table 1. Properties of the water-/oil-/gas-saturated media.

Property	Value
K_s (GPa)	35
K_m (GPa)	7
K_f (GPa)	2.4/2.1/0.0056
μ (GPa)	5.5
φ	0.25/0.25/0.1
ρ_s (g/m^3)	2.65
ρ_f (g/m^3)	1.0/0.7/0.14
φ	0.1
κ (Darcy)	1
ς	2
η ($\times 10^{-3}$) (Pa·s)	1/4/0.22
β ($\times 10^6$) (kg/(m·s^2·K))	2.1
β_f ($\times 10^6$) (kg/(m·s^2·K))	0.7/1.5/1.2
C_s ($\times 10^6$) (kg/(m·s^2·K))	2.4
C_f ($\times 10^3$) (kg/(m·s^2·K))	4.18/2.88/1.47
γ_s (m·kg /(s^3·K))	12
γ_f (m·kg /(s^3·K))	8.76/8.45/7.79
T_0 (K)	400
α_s ($\times 10^{-4}$) (K^{-1})	2.4
α_f ($\times 10^{-4}$) (K^{-1})	7/5/20
α_{fs} ($\times 10^{-4}$) (K^{-1})	−2.4/−1.6/−9.7

The attenuation is related to the classical Biot and thermal diffusion loss mechanisms. The global Biot flux dominates the fast P wave in Figure 1. As shown in Figure 1a, there are three peaks in the fast P-wave attenuation, with the two peaks at higher frequencies corresponding to the fast and slow thermal waves. In the TT-DPL model, the high-frequency sensitivity of the two thermal peaks of the fast P wave increases systematically, especially that of the fast T wave. In contrast, the slow thermal peak of the slow P wave becomes more sensitive. According to the Biot theory, the slow P wave is influenced by fluid flow, the slow T wave is influenced by heat conduction in the fluid, and the fast T wave is influenced by heat conduction in the solid. If the relaxation times on the right side of the heat conduction equation differ, the P wave experiences stronger dispersion and attenuation at high frequencies, whereas the T wave shows the opposite behavior. Because the relaxation time of the temperature term is shorter than that of the displacement term, the overall temperature reaches thermal equilibrium faster.

Figures 2 and 3 show the dispersion and attenuation curves for the four P waves and S waves in different fluid-saturated media, respectively. The fluid has a minor effect on the fast T wave, with the difference in the limiting velocity being less than 50 m/s. However, the velocity and attenuation frequency of the slow T wave are significantly affected by the fluid, confirming that the slow T wave is primarily influenced by the fluid. In Figure 2a, the frequencies of the Biot peak (approximately 10 kHz) and the fast T peak (approximately 10 GHz) are basically the same, with the slow T-wave peak frequency following the order: gas > water > glycerol. The two thermal peaks in the gas-saturated rock almost coincide in frequency, resulting in a single thermal peak on the attenuation curve.

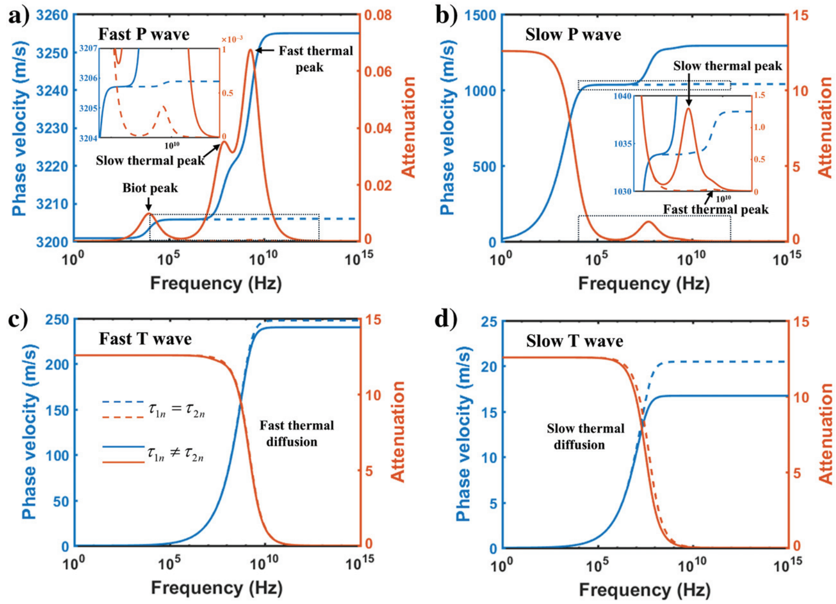

Figure 1. The phase velocities (the blue lines) and attenuation factors (the orange lines) of (a) fast P, (b) slow P, (c) fast T, and (d) slow T waves as a function of frequency. The relaxation times are $\tau_{1s}/\tau_{1f} = 0.08/25$ ns, $\tau_{2s}/\tau_{2f} = 0.24/7.5$ ns (the solid line), and $\tau_{2s}/\tau_{2f} = \tau_{1s}/\tau_{1f}$ (the dashed line).

Figure 3 shows that the fluid affects the velocity dispersion and attenuation frequency of the S wave. The attenuation corresponds to a Biot peak because no heat-related properties are involved. The combined effects of porosity, fluid density, viscosity, and other properties result in the wave velocity of gas-saturated rocks being higher than that of oil- and water-saturated rocks.

Typically, the relaxation time of the fluid phase is considered to be larger than that of the solid phase (Liu et al., 2023), with the relaxation time coefficient $E = \tau_{1s}/\tau_{1f} \approx 30$ for water-saturated rocks according to the relaxation times in Figure 1. The decrease in E implies that the difference in relaxation times between the fluid and solid phases diminishes, causing the entire medium to reach thermal equilibrium in a shorter time. We change the value of E in Figure 4, however, such a large change rarely occurs in real water-saturated rocks, which mainly demonstrates how the physical behavior changes with differences in relaxation times. The results show that the limiting velocity of the P wave remains unchanged as E decreases, and only the characteristic frequencies corresponding to the two thermal wave peaks gradually converge. Physically, changes in the ratio of fluid-solid relaxation times in water-saturated rocks do not affect heat conversion and dissipation during P-wave propagation. Because the decrease in E is achieved by reducing the fluid relaxation time, the fluid transfers the same amount of heat in less time, causing the limiting velocity of the slow T wave to increase. In addition, in the TT-DPL model, $D = \tau_{2n}/\tau_{1n}(n = s, f)$, and in the TT-SPL model, $D = 1$. It can be viewed as the interaction between fluid and solid heat transfer in saturated rock. The limiting velocity and the peak attenuation value of the P wave increase with an increase in D, whereas the T waves decrease gradually, and the peak frequency of all waves remains relatively constant. The complexity of the energy exchange or medium inhomogeneity in fluid-saturated rocks results in increased attenuation, whereas the proportion of thermal energy in the dissipated part decreases.

Next, we compute the snapshots of the wavefield using the RSG-FD method, with 501 grid points along the vertical and horizontal directions. The source is a Ricker wavelet located at the center of the mesh, at coordinates [251,251]. The source time history is

$$w(t) = \cos[2\pi(t - t_0)f_0]\exp[-2(t - t_0)^2 f_0^2], \tag{16}$$

where $t_0 = 3/(2f_0)$ is the delay time, and f_0 is the dominant frequency of the wave.

We assume a grid size of $dx = dz = 0.3$ mm, a time step of $dt = 10$ ns, and a dominant source frequency of 10^{12} Hz. The signals along the vertical and horizontal directions from the source are shown in Figure 5. The four P-wave velocities in Figure 1 generally agree with the calculated results shown in Figure 5. The P-wave velocities are 3206 and 1112 m/s, respectively. The slight difference is due to errors in waveform extraction from the wavefield snapshots. Heat waves are difficult to capture accurately in the signal due to the attenuation effect and the low speed of the slow T wave. The calculated heat wave velocity lies within the range of the two T-wave velocities. When the fluid-related parameters are excluded from the TT-DPL model, the results become equivalent to those of the ST-STL model. Figure 6a shows a snapshot for the simplified fluid term model, yielding results identical to those of the thermoelastic model described in Hou et al. (2021b). Only elastic waves

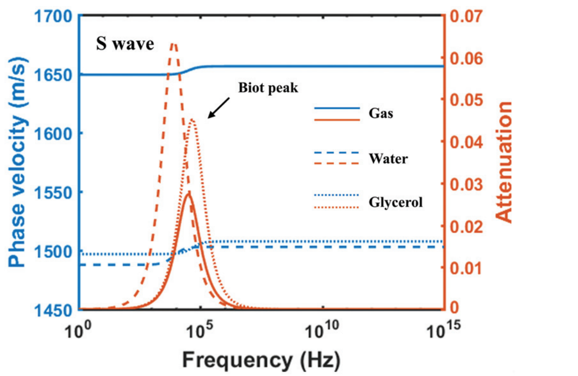

Figure 3. The phase velocities (the blue lines) and attenuation factors (the orange lines) of S waves as a function of frequency. The properties are the same as shown in Figure 2.

Figure 2. The phase velocities (the blue lines) and attenuation factors (the orange lines) of (a) fast P, (b) slow P, (c) fast T, and (d) slow T waves as a function of frequency calculated using the TT model for gas-saturated (the solid lines), water-saturated (the dashed lines), and glycerol-saturated (the dotted lines) rocks. The fluid relaxation times for gas, water, and glycerol-saturated rocks are τ_{mf} = 4, 2.5, and 1.6 ns, respectively.

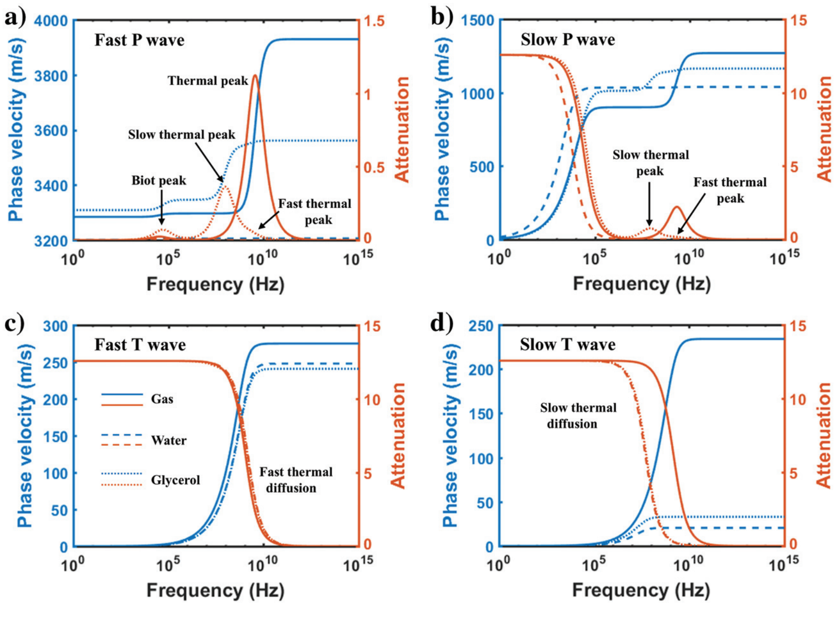

are observable in the wavefield simulation, which further confirms that the TT-DPL model simplifies to thermoelastic theory.

Figure 7 shows v_x snapshots corresponding to the TT-SPL model at two different times, wherein we observe the propagating fast P, slow P, and fast T waves. Attenuation causes the amplitude of the fast T wave to be significantly smaller than that of the P waves. Magnifying the 1.6 ms snapshot reveals the presence of an almost diffusive slow T wave. This is more clearly observed in the q_z component in Figure 8b. Figure 8 shows snapshots of different components: the P and slow T waves in the x-z stress and the fast P and fast T waves in the fluid pressure. The amplitude of the thermal wave is stronger than that of the P waves in the particle velocity snapshots q_z relative to the solid phase. In addition, the temperature field is more sensitive to differences between the solid and fluid phases.

Figure 9 compares snapshots of different fluid-saturated rocks. The velocities of the fast P wave and the slow T wave are highest in gas-saturated rocks. However, the strong attenuation of the fast P wave means that no waveforms are visible in the snapshots, whereas the slow T wave is the fastest. The attenuation of the slow P wave is almost zero at high frequency, and the velocities follow this order: gas saturated > glycerol saturated > water saturated, which is consistent with the plane-wave analysis. Glycerol-saturated rock exhibits minimal attenuation near the dominant frequency, which hides the T wave compared to the P wave. This study enhances our understanding of energy conversion and heat transfer during seismic wave propagation in porous rocks. However, the application of slow P waves and T waves in practical geophysical exploration still faces several challenges. For instance, the physical properties of rocks vary significantly under different stratigraphic temperatures and pressures, leading to errors in velocity calculations. The variable properties thermoporoelastic model offers the potential for reservoir temperature and pressure inversion.

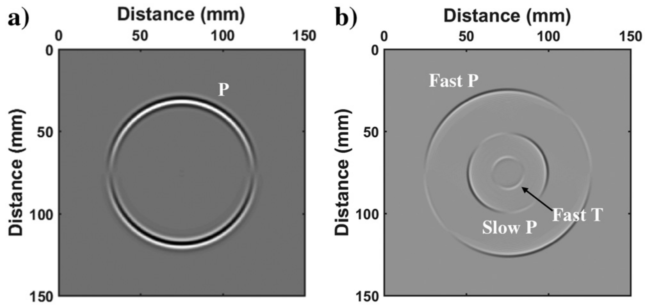

Figure 6. Snapshots of the particle velocity v_z at 1.6 ms of (a) the ST-SPL model and (b) the TT-DPL model. The properties used are the same as those of the TT model in Figure 1.

Figure 4. The phase velocity (the blue line) and attenuation factors (the orange line) as a function of frequency for (a) fast P, (b) slow P, (c) fast T, and (d) slow T waves calculated using the TT-DPL model with different relaxation times.

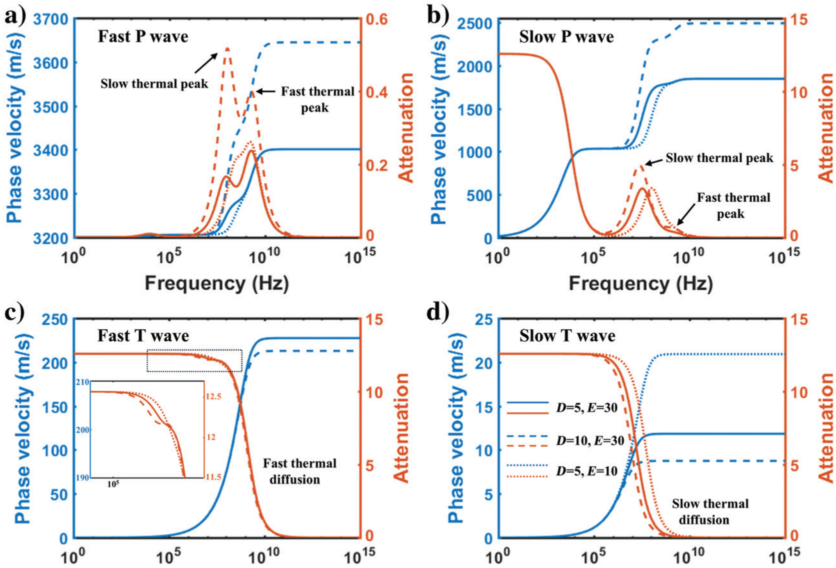

Figure 5. (a) Horizontal and vertical signals and (b) velocity comparisons at 1.6 ms. The parameters correspond to the TT model shown in Figure 1.

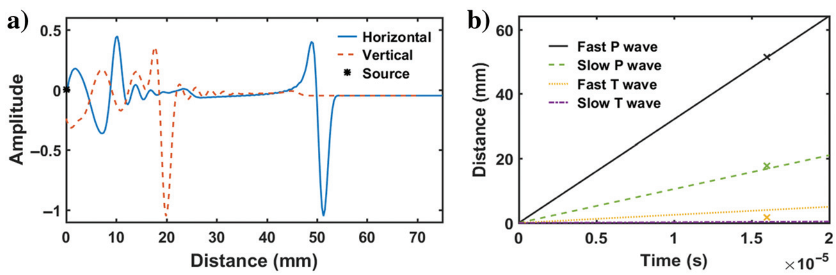

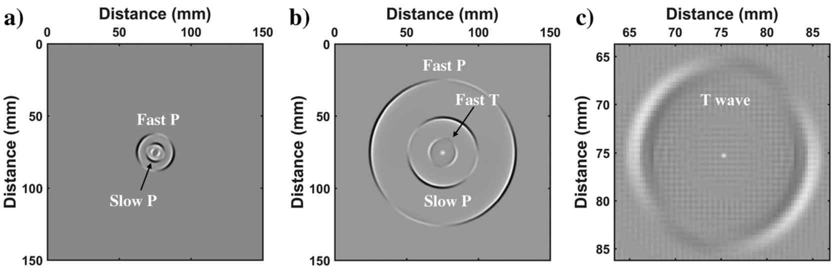

Figure 7. Snapshots of the particle velocity v_x at (a) 0.4 ms and (b) 1.6 ms, with (c) showing a blow-up of (b). The properties used are the same as those of the TT model in Figure 1.

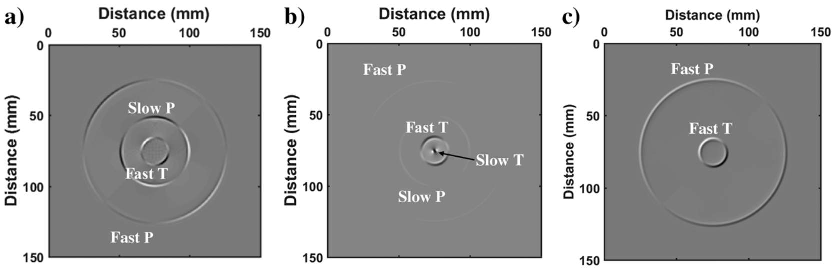

Figure 8. Snapshots of (a) the *x-z* stress τ_{xz}, (b) the particle velocity of the fluid relative to the solid q_z, and (c) the pressure of the fluid p at 1.6 ms. The parameters used are identical to those of the TT model in Figure 1.

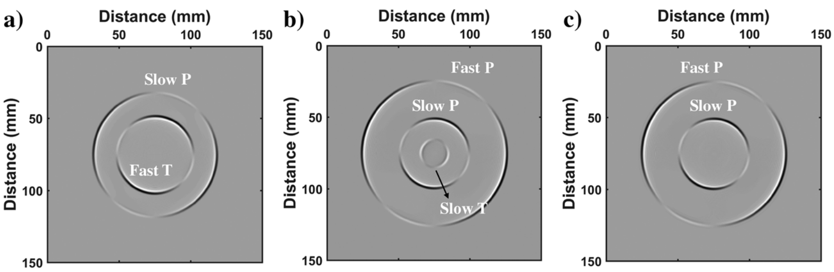

Figure 9. Snapshots of the particle velocity v_x at 1.6 ms in (a) gas-saturated, (b) water-saturated, and (c) glycerol-saturated rocks. The properties used are the same as those of the TT model in Figure 2.

CONCLUSION

We present the analytical results and numerical simulations of plane waves propagating in thermoporoelastic media with two temperatures. The theory describes the coupling of the solid and fluid phases, their different temperatures, and their distinct relaxation times (lags) for displacement and temperature. An analysis of the plane waves results in four P waves and one S wave. The different lag times lead to additional dispersion and attenuation at high frequencies. The effects of fluid type are most pronounced for the slow P and T waves, whereas the low-frequency Biot mechanism is more strongly influenced by the solid phase. As the ratio of relaxation times increases, the two peaks of T wave damping gradually separate, resulting in stronger dissipation.

We then perform numerical simulations using an FD algorithm based on a time-splitting algorithm. This method offers significant advantages in the treatment of the spatial inhomogeneities of the medium and in overcoming stability problems. The fluid phase has a strong influence on high-frequency anelastic effects, as can be seen in the snapshots, and the presence of thermal waves is more evident in the fluid components of the wavefield.

ACKNOWLEDGMENTS

This work was supported in part by the National Natural Science Foundation of China under grant no. 42230803 and the 111 Project, “Deep-Superdeep Oil and Gas Geophysical Exploration,” under grant no. B18055.

DATA AND MATERIALS AVAILABILITY

Data associated with this research are available and can be obtained by contacting the corresponding author.

APPENDIX A

PLANE-WAVE ANALYSIS

To investigate the characteristics of wave propagation in thermoporoelastic media, we consider the following homogeneous plane-wave expressions:

$$\begin{cases} u_i = A_s^{\mathrm{P}} \exp\left[-i\omega\left(t - \frac{l_j}{v_c}x_j\right)\right] \\ w_i = A_f^{\mathrm{P}} \exp\left[-i\omega\left(t - \frac{l_j}{v_c}x_j\right)\right] \\ T_s = B_s^{\mathrm{P}} \exp\left[-i\omega\left(t - \frac{l_j}{v_c}x_j\right)\right] \\ T_f = B_f^{\mathrm{P}} \exp\left[-i\omega\left(t - \frac{l_j}{v_c}x_j\right)\right] \end{cases}, \tag{A-1}$$

where A and B are the amplitude constants, superscript P is the compression wave, ω is the angular frequency, v_c is the complex velocity, l_j denotes the propagation directions, x_j represents the position components, and $i = \sqrt{-1}$.

For S waves, the propagation direction is perpendicular to the displacement vector, and we have

$$\begin{cases} \mu\Upsilon_{s,ii} = \rho\ddot{\Upsilon}_s + \rho_f\ddot{\Upsilon}_f \\ \rho_f\ddot{\Upsilon}_s + m\ddot{\Upsilon}_f + r\dot{\Upsilon}_f = 0 \end{cases}, \tag{A-2}$$

and solving equation A-3 yields

$$v_c^2(\mathrm{Swave}) = \left[\frac{\rho}{\mu} - \frac{\omega\rho_f^2}{\mu(m\omega + ir)}\right]^{-\frac{1}{2}}. \tag{A-3}$$

We can see that the propagation of S waves is independent of the thermal properties in isotropic homogeneous media.

For P waves, the propagation direction is parallel to the displacement vector. The dispersion relation is

$$A(v_c^2)^4 + B(v_c^2)^3 + C(v_c^2)^2 + Dv_c^2 + E = 0, \tag{A-4}$$

where

$$\begin{cases} A = \tau_{1f}\tau_{1s}d_3c_3\omega^5 \\ B = \{iT_0[\omega(b_2+b_3)-(m\omega+ir)(b_4-b_5)]+b_6\}\omega^3 \\ C = [c_4+iT_0(c_5+c_6+c_7+c_8)-(\lambda+2\mu)Md_3\tau_{1f}\tau_{1s}-\omega c_3\gamma_s'\gamma_f'+d_1d_2]\omega^2, \\ D = \{-d_1\gamma_s'\gamma_f'-(\lambda+2\mu)Md_2+iT_0[(\lambda+2\mu+\alpha^2M)d_4+M(d_5+d_6)]\}\omega \\ E = (\lambda+2\mu)M\gamma_s'\gamma_f' \end{cases} \tag{A-5}$$

with

$$\begin{aligned} b_1 &= (R_{11}R_{22}+R_{12}R_{21})\rho_f - R_{21}R_{22}\rho \\ b_2 &= \tau_{2s}\tau_{1f}[F_{22}R_{21}(R_{21}\rho - 2R_{11}\rho_f) + b_1F_{21}] \\ b_3 &= \tau_{1s}\tau_{2f}[F_{11}R_{22}(R_{22}\rho - 2R_{12}\rho_f) + b_1F_{12}] \\ b_4 &= \tau_{2s}\tau_{1f}R_{11}(F_{21}R_{12} - F_{22}R_{11}) \\ b_5 &= \tau_{2f}\tau_{1s}R_{12}(F_{11}R_{12} - F_{12}R_{11}) \\ b_6 &= \tau_{1s}\tau_{1f}d_3 + \omega c_3 d_2 \\ c_1 &= F_{21}R_{21} - F_{11}R_{22}, \\ c_2 &= F_{12}R_{22} - F_{22}R_{21}, \\ c_3 &= \omega\rho_f^2 - (m\omega+ir)\rho \\ c_4 &= -\tau_{2f}\tau_{2s}T_0^2(R_{11}R_{22} - R_{12}R_{21})^2 \\ c_5 &= \tau_{2f}\{R_{22}^2[-(\lambda+2\mu+\alpha^2M)\tau_{1s}F_{11} - \omega\rho\gamma_s'] \\ &\quad + 2R_{22}R_{12}(\alpha M\tau_{1s}F_{11} + \omega\rho_f\gamma_s') \\ &\quad - R_{12}^2[M\tau_{1s}F_{11} + (m\omega+ir)\gamma_s']\} \\ c_6 &= \tau_{2s}\{R_{21}^2[-(\lambda+2\mu+\alpha^2M)\tau_{1f}F_{22} - \omega\rho\gamma_f'] \\ &\quad + 2R_{21}R_{11}(\alpha M\tau_{1f}F_{22} + \omega\rho_f\gamma_f') \\ &\quad - R_{11}^2[M\tau_{1f}F_{22} + (m\omega+ir)\gamma_f']\} \\ c_7 &= \tau_{1f}\tau_{2s}F_{21}\{[(-\alpha R_{22}+R_{12})R_{11} - \alpha R_{12}R_{21}]M \\ &\quad + R_{21}R_{22}(\lambda+2\mu+\alpha^2M)\} \\ c_8 &= \tau_{1s}\tau_{2f}F_{21}\{[(-\alpha R_{22}+R_{12})R_{11} - \alpha R_{12}R_{21}]M \\ &\quad + R_{21}R_{22}(\lambda+2\mu+\alpha^2M)\} \\ d_1 &= -\omega M(2\alpha\rho_f - \rho) + (\lambda+2\mu+\alpha^2M)(m\omega+ir) \\ d_2 &= \tau_{1s}F_{11}\gamma_f' + \tau_{1f}F_{22}\gamma_s', \\ d_3 &= F_{12}F_{21} - F_{11}F_{22}, \\ d_4 &= \tau_{2s}R_{21}^2\gamma_f' + \tau_{2f}R_{22}^2\gamma_s' \\ d_5 &= \tau_{2s}R_{11}\gamma_f'(R_{11} - 2\alpha R_{21}), \\ d_6 &= \tau_{2f}R_{12}\gamma_s'(R_{12} - 2\alpha R_{22}). \end{aligned} \tag{A-6}$$

The phase velocity and attenuation factor of the P waves are (Hou et al., 2022)

$$V_{\mathrm{P}} = \left[\mathrm{Re}\left(\frac{1}{v_c}\right)\right]^{-1}, \quad A = -\omega\,\mathrm{Im}\left(\frac{1}{v_c}\right). \tag{A-7}$$

APPENDIX B

SPLITTING ALGORITHM

The time integration from t to $t + dt$ for the stiff matrix is solved analytically to obtain the intermediate solution,

$$\begin{cases} \dot{v}_x = -\frac{\eta}{\kappa}\beta_{12}q_x, \dot{v}_z = -\frac{\eta}{\kappa}\beta_{12}q_z \\ \dot{q}_x = -\frac{\eta}{\kappa}\beta_{22}q_x, \dot{q}_z = -\frac{\eta}{\kappa}\beta_{22}q_z \\ \dot{\sigma}_{xx} = \dot{\sigma}_{zz} = -R_{11}\psi_s - R_{12}\psi_f \\ \dot{p} = R_{21}\psi_s + R_{22}\psi_f \\ \dot{\psi}_s = A_0(-F_{12}F_{21}\tau_s + F_{11}F_{22}\tau_f)\psi_s + A_0(-F_{12}F_{22}\tau_s + F_{12}F_{22}\tau_f)\psi_f \\ \dot{\psi}_f = A_0(F_{11}F_{21}\tau_s - F_{11}F_{21}\tau_f)\psi_s + A_0(F_{11}F_{22}\tau_s - F_{12}F_{21}\tau_f)\psi_f \end{cases}, \tag{B-1}$$

where $A_0 = [\tau_s\tau_f(F_{12}F_{21} - F_{11}F_{22})]^{-1}$.

We obtain

$$\begin{cases} v_x* = v_x^n + \frac{\beta_{12}}{\beta_{22}}[\exp(\lambda_s dt)-1]q_x^n, v_z* = v_z^n + \frac{\beta_{12}}{\beta_{22}}[\exp(\lambda_s dt)-1]q_z^n \\ q_x* = \exp(\lambda_s dt)q_x^n, q_z* = \exp(\lambda_s dt)q_z^n \\ \sigma_{xx}* = \sigma_{xx}^n - \frac{R_{11}}{p+n}[\exp(\lambda_1 dt)+\exp(\lambda_2 dt)-1]\psi_s^n - \frac{R_{12}}{p+n}\left[\frac{\lambda_1-p}{q}\exp(\lambda_1 dt)+\frac{\lambda_2-p}{q}\exp(\lambda_2 dt)-1\right]\psi_f^n \\ \sigma_{zz}* = \sigma_{zz}^n - \frac{R_{11}}{p+n}[\exp(\lambda_1 dt)+\exp(\lambda_2 dt)-1]\psi_s^n - \frac{R_{12}}{p+n}\left[\frac{\lambda_1-p}{q}\exp(\lambda_1 dt)+\frac{\lambda_2-p}{q}\exp(\lambda_2 dt)-1\right]\psi_f^n \\ p* = p^n + \frac{R_{21}}{p+n}[\exp(\lambda_1 dt)+\exp(\lambda_2 dt)-1]\psi_s^n + \frac{R_{22}}{p+n}\left[\frac{\lambda_1-p}{q}\exp(\lambda_1 dt)+\frac{\lambda_2-p}{q}\exp(\lambda_2 dt)-1\right]\psi_f^n \\ \psi_s* = [\exp(\lambda_1 dt)+\exp(\lambda_2 dt)]\psi_s^n \\ \psi_f* = \left[\frac{\lambda_1-p}{q}\exp(\lambda_1 dt)+\frac{\lambda_2-p}{q}\exp(\lambda_2 dt)\right]\psi_f^n \end{cases}, \tag{B-2}$$

where

$$\begin{cases} \lambda_1 = \left[A_0(\tau_s+\tau_f)(F_{11}F_{22}-F_{12}F_{21}) + A_0(\tau_f-\tau_s)\sqrt{F_{11}^2F_{22}^2 - F_{12}^2F_{21}^2}\right]/2 \\ \lambda_2 = \left[A_0(\tau_s+\tau_f)(F_{11}F_{22}-F_{12}F_{21}) - A_0(\tau_f-\tau_s)\sqrt{F_{11}^2F_{22}^2 - F_{12}^2F_{21}^2}\right]/2 \\ p = A_0(F_{11}F_{22}\tau_f - F_{12}F_{21}\tau_s), q = A_0F_{11}F_{22}(\tau_f-\tau_s), n = A_0(F_{11}F_{22}\tau_s - F_{12}F_{21}\tau_f) \end{cases}. \tag{B-3}$$

For time stepping, we use the time-splitting algorithm of Carcione et al. (2019). Discretizing time as $t = ndt$, it shows that

$$\begin{cases} v_x^{n+1} = v_x* + dt[\beta_{11}(\partial_x\sigma_{xx}* + \partial_z\sigma_{xz}^n) - \beta_{12}(\partial_x p* + rq_x*)] \\ v_z^{n+1} = v_z* + dt[\beta_{11}(\partial_x\sigma_{xz}^n + \partial_z\sigma_{zz}*) - \beta_{12}(\partial_z p* + rq_z*)] \\ q_x^{n+1} = q_x* + dt[\beta_{21}(\partial_x\sigma_{xx}* + \partial_z\sigma_{xz}^n) - \beta_{22}(\partial_x p* + rq_x*)] \\ q_z^{n+1} = q_z* + dt[\beta_{21}(\partial_x\sigma_{xz}^n + \partial_z\sigma_{zz}*) - \beta_{22}(\partial_z p* + rq_z*)] \\ \sigma_{xx}^{n+1} = \sigma_{xx}* + dt[(\lambda+2\mu)\partial_x v_x* + \lambda\partial_z v_z* + \alpha^2M(\partial_x v_x* + \partial_z v_z*) + \alpha M(\partial_x q_x* + \partial_z q_z*) - R_{11}\psi_s* - R_{12}\psi_f*] \\ \sigma_{zz}^{n+1} = \sigma_{zz}* + dt[(\lambda+2\mu)\partial_z v_z* + \lambda\partial_x v_x* + \alpha^2M(\partial_x v_x* + \partial_z v_z*) + \alpha M(\partial_x q_x* + \partial_z q_z*) - R_{11}\psi_s* - R_{12}\psi_f*] \\ \sigma_{xz}^{n+1} = \sigma_{xz}^n + dt[\mu(\partial_x v_x* + \partial_z v_z*)] \\ p^{n+1} = p* + dt[-\alpha M(\partial_x v_x* + \partial_z v_z*) - M(\partial_x q_x* + \partial_z q_z*) + R_{21}\psi_s* + R_{22}\psi_f*] \\ T_s^{n+1} = T_s^n + dt(\psi_s*) \\ T_f^{n+1} = T_f^n + dt(\psi_f*) \\ \psi_s^{n+1} = \psi_s* + dt\left\{A_0 \times \begin{cases} F_{12}\tau_s\left[\gamma_f'(\partial_{xx}\psi_f* + \partial_{zz}\psi_f*) - F_{21}\psi_s* - F_{22}\psi_f* - T_0\begin{pmatrix} R_{12}(\partial_x v_x* + \partial_z v_z* + \tau_f(\partial_x\Pi_x* + \partial_z\Pi_z*)) \\ +R_{22}(\partial_x q_x* + \partial_z q_z* + \tau_f(\partial_x\Omega_x* + \partial_z\Omega_z*)) \end{pmatrix}\right] \\ -F_{22}\tau_f\left[\gamma_s'(\partial_{xx}\psi_s* + \partial_{zz}\psi_s*) - F_{11}\psi_s* - F_{12}\psi_f* - T_0\begin{pmatrix} R_{11}(\partial_x v_x* + \partial_z v_z* + \tau_s(\partial_x\Pi_x* + \partial_z\Pi_z*)) \\ +R_{21}(\partial_x q_x* + \partial_z q_z* + \tau_s(\partial_x\Omega_x* + \partial_z\Omega_z*)) \end{pmatrix}\right] \end{cases}\right\} \\ \psi_f^{n+1} = \psi_f* + dt\left\{A_0 \times \begin{cases} -F_{11}\tau_s\left[\gamma_f'(\partial_{xx}\psi_f* + \partial_{zz}\psi_f*) - F_{21}\psi_s* - F_{22}\psi_f* - T_0\begin{pmatrix} R_{12}(\partial_x v_x* + \partial_z v_z* + \tau_f(\partial_x\Pi_x* + \partial_z\Pi_z*)) \\ +R_{22}(\partial_x q_x* + \partial_z q_z* + \tau_f(\partial_x\Omega_x* + \partial_z\Omega_z*)) \end{pmatrix}\right] \\ +F_{21}\tau_f\left[\gamma_s'(\partial_{xx}\psi_s* + \partial_{zz}\psi_s*) - F_{11}\psi_s* - F_{12}\psi_f* - T_0\begin{pmatrix} R_{11}(\partial_x v_x* + \partial_z v_z* + \tau_s(\partial_x\Pi_x* + \partial_z\Pi_z*)) \\ +R_{21}(\partial_x q_x* + \partial_z q_z* + \tau_s(\partial_x\Omega_x* + \partial_z\Omega_z*)) \end{pmatrix}\right] \end{cases}\right\} \end{cases}, \tag{B-4}$$

where

$$\begin{cases} \Pi_x* = \beta_{11}(\partial_x\sigma_{xx}* + \partial_z\sigma_{xz}^n) - \beta_{12}(\partial_x p* + rq_x*) \\ \Pi_z* = \beta_{11}(\partial_x\sigma_{xz}^n + \partial_z\sigma_{zz}*) - \beta_{12}(\partial_z p* + rq_z*) \\ \Omega_x* = \beta_{21}(\partial_x\sigma_{xx}* + \partial_z\sigma_{xz}^n) - \beta_{22}(\partial_x p* + rq_x*) \\ \Omega_z* = \beta_{21}(\partial_x\sigma_{xz}^n + \partial_z\sigma_{zz}*) - \beta_{22}(\partial_z p* + rq_z*) \end{cases}, \tag{B-5}$$

where the eighth- and second-order FD approximations are used for the spatial and temporal derivatives, respectively. The variables marked with an asterisk correspond to the intermediate solutions at each time step, as shown in equation B-2.

REFERENCES

Abd-Alla, A. M., S. M. Abo-Dahab, and A. A. Kilany, 2020, Effect of several fields on a generalized thermoelastic medium with voids in the context of Lord-Shulman or dual-phase-lag models: Mechanics Based Design of Structures and Machines, **50**, 3901–3924, doi: 10.1080/15397734.2020.1823852.

Armstrong, B. H., 1984, Models for thermoelastic attenuation of waves in heterogeneous solids: Geophysics, **49**, 1032–1040, doi: 10.1190/1.1441718.

Batzle, M. L., and Z. Wang, 1992, Seismic properties of pore fluids: Geophysics, **57**, 1396–1408, doi: 10.1190/1.1443207.

Breede, K., K. Dzebisashvili, X. Liu, and G. Falcone, 2013, A systematic review of enhanced (or engineered) geothermal systems: Past, present and future: Geothermal Energy, **1**, 1–27, doi: 10.1186/2195-9706-1-4.

Carcione, J. M., 2022, Wave fields in real media. Theory and numerical simulation of wave propagation in anisotropic, anelastic, porous and electromagnetic media, 4th ed.: Elsevier.

Carcione, J. M., F. Cavallini, E. J. Wang, J. Ba, and L.-Y. Fu, 2019, Physics and simulation of wave propagation in linear thermo-poroelastic media: Journal Geophysics Research, **124**, 8147–8166, doi: 10.1029/2019JB017851.

Carcione, J. M., and G. Quiroga-Goode, 1995, Some aspects of the physics and numerical modeling of Biot compressional waves: Journal of Computational Acoustics, **3**, 261–280, doi: 10.1142/S0218396X95000136.

Carcione, J. M., and G. Seriani, 2001, Wave simulation in frozen porous media: Journal of Computational Physics, **170**, 676–695, doi: 10.1006/jcph.2001.6756.

Carcione, J. M., Z.-W. Wang, W. Ling, E. Salusti, J. Ba, and L.-Y. Fu, 2018, Simulation of wave propagation in linear thermoelastic media: Geophysics, **84**, no. 1, T1–T11, doi: 10.1190/geo2018-0448.1.

Cheng, Y. F., L.-Y. Fu, W. T. Hou, J. M. Carcione, W. B. Deng, and Z. W. Wang, 2024, Thermo-poroelastic AVO modeling of Olkaria geothermal reservoirs: Geoenergy Science and Engineering, **241**, 213166, doi: 10.1016/j.geoen.2024.213166.

Cui, X., and L. N. Y. Wong, 2021, A 3D thermo-hydro-mechanical coupling model for enhanced geothermal systems: International Journal of Rock Mechanics and Mining Sciences, **143**, 104744, doi: 10.1016/j.ijrmms.2021.104744.

Faccioli, E., F. Maggio, R. Paolucci, and A. Quarteroni, 1997, 2D and 3D elastic wave propagation by a pseudo-spectral domain decomposition method: Journal of Seismology, **1**, 237–251, doi: 10.1023/A:1009758820546.

Fu, L.-Y., 2017, Deep-superdeep oil & gas geophysical exploration 111: Program report jointly initiated by MOE and SAFEA, B18055, School of Geosciences, China University of Petroleum (East China).

Fu, L.-Y., 2019, Geophysical characterization of Olkaria geothermal reservoirs in Kenya: Technical Report, CNPC Greatwall Drilling Engineering Company Ltd.

Fu, L.-Y., and Y. G. Mou, 1994, Boundary element method for elastic wave forward modeling: Chinese Journal of Geophysics, **37**, 521–529.

Han, D. H., J. Liu, and M. Baztle, 2008, Seismic properties of heavy oils: Measured data: The Leading Edge, **27**, 1108–1115, doi: 10.1190/1.2978972.

Hou, W., L.-Y. Fu, J. M. Carcione, Z. W. Wang, and J. Wei, 2021a, Simulation of thermoelastic waves based on the Lord-Shulman theory: Geophysics, **86**, no. 3, T155–T164, doi: 10.1190/geo2020-0515.1.

Hou, W., L.-Y. Fu, J. Wei, and Z. W. Wang, 2021b, Characteristics of wave propagation in thermoelastic medium: Chinese Journal of Geophysics, **64**, 1364–1374, doi: 10.6038/cjg2021N0458.

Hou, W. T., L.-Y. Fu, and J. M. Carcione, 2023, Reflection and transmission of inhomogeneous plane waves in thermoporoelastic media: Surveys in Geophysics, **44**, 1897–1917, doi: 10.1007/s10712-023-09782-z.

Hou, W. T., L.-Y. Fu, and J. M. Carcione, 2024, Reflection, transmission and AVO response of inhomogeneous plane waves in thermoporoelastic media with two-temperature equations of heat conduction: Geophysics, **89**, no. 1, MR297–MR307, doi: 10.1190/geo2023-0625.1.

Hou, W. T., L.-Y. Fu, J. M. Carcione, and T. C. Han, 2022, Reflection and transmission of inhomogeneous plane waves in thermoelastic media: Frontiers in Earth Science, **10**, 1–16, doi: 10.3389/feart.2022.850331.

Hu, S. Z., L.-Y. Fu, and Z. L. Pei, 2009, A boundary element method for the 2D wave equation in fluid-saturated porous media: Chinese Journal of Geophysics, **52**, 2364–2369, doi: 10.3969/j.issn.0001-5733.2009.09.022.

Jacquey, A. B., M. Cacace, G. Blöcher, and M. Scheck-Wenderoth, 2015, Numerical investigation of thermoelastic effects on fault slip tendency during injection and production of geothermal fluids: Energy Procedia, **76**, 311–320, doi: 10.1016/j.egypro.2015.07.868.

Jian, S. K., L.-Y. Fu, Z. H. Liao, W. B. Deng, and Q. Z. Du, 2022, Elastic characteristics of fault damage zones within superdeep carbonates in Tarim Basin, Northwest China: Journal of Geophysics and Engineering, **19**, 650–662, doi: 10.1093/jge/gxac040.

Kaminski, W., 1990, Hyperbolic heat conduction equation for materials with a nonhomogeneous inner structure: ASME Journal of Heat and Mass Transfer, **112**, 555–560, doi: 10.1115/1.2910422.

Kjartansson, E., 1979, Attenuation of seismic waves in rocks and applications in energy exploration: Ph.D. thesis, Stanford University.

Komatitsch, D., and R. Martin, 2007, An unsplit convolutional perfectly matched layer improved at grazing incidence for the seismic wave equation: Geophysics, **72**, no. 1, SM155–SM167, doi: 10.1190/1.2757586.

Kumar, M., J. Bhagwan, P. Kaswan, X. Liu, and M. Kumari, 2023, Inhomogeneous waves propagation in double-porosity thermoelastic media: International Journal of Numerical Methods for Heat and Fluid Flow, **33**, 2927–2962, doi: 10.1108/HFF-03-2023-0146.

Kumar, M., X. Liu, M. Kumari, and P. Yadav, 2022, Wave propagation at the welded interface of an elastic solid and unsaturated poro-thermoelastic solid: International Journal of Numerical Methods for Heat and Fluid Flow, **32**, 3526–3550, doi: 10.1108/HFF-01-2022-0008.

Kumar, M., L. Priyanka, L.-Y. Fu, K. Neelam, K. Pradeep, and N. Q. Li, 2024, Rayleigh-type wave in thermoporoelastic media with dual-phase-lag heat conduction: International Journal of Numerical Methods for Heat and Fluid Flow, **35**, 774–798, doi: 10.1108/HFF-11-2024-0853.

Kumar, R., R. Vohra, and M. G. Gorla, 2017, Variational principle and plane wave propagation in thermoelastic medium with double porosity under Lord-Shulman theory: Journal of Solid Mechanics, **9**, 423–433.

Li, N. Q., L.-Y. Fu, W. B. Deng, J. M. Carcione, and J. Yang, 2023, A thermo-hydro-mechanical model to evaluate the seismic properties of geothermal reservoirs: Geophysics, **88**, no. 1, WB23–WB35, doi: 10.1190/geo2022-0491.1.

Li, N. Q., L.-Y. Fu, J. Yang, and T. Han, 2021, On three-stage temperature dependence of elastic wave velocities for rocks: Journal of Geophysics and Engineering, **18**, 328–338, doi: 10.1093/jge/gxab017.

Liu, H., G. Dai, F. Zhou, and X. Cao, 2022, A mixture theory analysis for reflection phenomenon of homogeneous plane-P1-wave at the boundary of unsaturated porothermoelastic media: Geophysical Journal International, **228**, 1237–1259, doi: 10.1093/gji/ggab379.

Liu, Y. F., L.-Y. Fu, W. B. Deng, W. T. Hou, J. M. Carcione, and J. Wei, 2023, Simulation of wave propagation in thermoporoelastic media with dual-phase-lag heat conduction: Journal of Thermal Stresses, **46**, 620–638, doi: 10.1080/01495739.2023.2193225.

Lord, H. W., and Y. Shulman, 1967, A generalized dynamical theory of thermoelasticity: Journal of the Mechanics and Physics of Solids, **15**, 299–309, doi: 10.1016/0022-5096(67)90024-5.

Mitra, K., S. Kumar, A. Vedavarz, and M. K. Moallemi, 1995, Experimental evidence of hyperbolic heat conduction in processed meat: ASME Journal of Heat and Mass Transfer, **117**, 568–573, doi: 10.1115/1.2822615.

Nield, D. A., and A. Bejan, 2006, Convection in porous media, 3rd ed.: Springer.

Noda, N., 1990, Thermal stress problem in a fluid- filled porous circular cylinder: Zeitschrift fur Angewandte Mathematik und Mechanik, **70**, 543–549, doi: 10.1002/zamm.19900701203.

Pecker, C., and H. Deresiewicz, 1973, Thermal effects on wave propagation in liquid filled porous media: Acta Mechanica, **16**, 45–64, doi: 10.1007/BF01177125.

Poletto, F., B. Farina, and J. M. Carcione, 2018, Sensitivity of seismic properties to temperature variations in a geothermal reservoir: Geothermics, **76**, 149–163, doi: 10.1016/j.geothermics.2018.07.001.

Rabbani, A., and D. R. Schmitt, 2018, Ultrasonic shear wave reflectometry applied to the determination of the shear moduli and viscosity of a viscoelastic bitumen: Fuel, **232**, 506–518, doi: 10.1016/j.fuel.2018.05.175.

Savage, J., 1966, Thermoelastic attenuation of elastic waves by cracks: Journal of Geophysical Research, **71**, 3929–3938, doi: 10.1029/JZ071i016p03929.

Schmitt, D. R., 1999, Seismic attributes for monitoring of a shallow heated heavy oil reservoir: A case study: Geophysics, **64**, 368–377, doi: 10.1190/1.1444541.

Serón, F. J., F. J. Sanz, M. Kindelan, and J. I. Badal, 1990, Finite-element method for elastic wave propagation: Communications in Applied Numerical Methods, **6**, 359–368, doi: 10.1002/cnm.1630060505.

Sharma, M. D., 2008, Wave propagation in thermoelastic saturated porous medium: Journal of Earth System Science, **117**, 951–958, doi: 10.1007/s12040-008-0080-4.

Singh, B., 2011, On propagation of plane waves in generalized porothermoelasticity: Bulletin of the Seismological Society of America, **101**, 756–762, doi: 10.1785/0120100091.

Treitel, S., 1959, On the attenuation of small-amplitude plane stress waves in a thermoelastic solid: Journal of Geophysical Research, **64**, 661–665, doi: 10.1029/JZ064i006p00661.

Tzou, D. Y., 1995a, A unified field approach for heat conduction from macro- to micro-scales: ASME Journal of Heat and Mass Transfer, **117**, 8–16, doi: 10.1115/1.2822329.

Tzou, D. Y., 1995b, The generalized lagging response in small-scale and high-rate heating: International Journal of Heat Mass Transfer, **38**, 3231–3240, doi: 10.1016/0017-9310(95)00052-B.

Vedavarz, A., K. Mitra, S. Kumar, and M. K. Moallemi, 1992, Effect of hyperbolic heat conduction on temperature distribution in laser irradiated tissue with blood perfusion: Advances in Biological Heat and Mass Transfer, **231**, 7–16.

Veres, I. A., T. Berer, and P. Burgholzer, 2013, Numerical modeling of thermoelastic generation of ultrasound by laser irradiation in the coupled thermoelasticity: Ultrasonics, **53**, 141–149, doi: 10.1016/j.ultras.2012.05.001.

Wang, E. J., J. M. Carcione, J. Ba, M. Alajmi, and A. N. Qadrouh, 2019, Nearly perfectly matched layer absorber for viscoelastic wave equations: Geophysics, **84**, no. 1, T335–T345, doi: 10.1190/geo2018-0732.1.

Wang, E. J., J. M. Carcione, Y. Yuan, and J. Ba, 2021, Reflection of inhomogeneous plane waves at the surface of a thermo-poroelastic medium: Geophysical Journal International, **224**, 1621–1639, doi: 10.1093/gji/ggaa543.

Wang, Z. W., L.-Y. Fu, S. K. Jian, and W. B. Deng, 2023, Application of a model-driven simultaneous prestack inversion of rock physical properties in ultra-deep Ordovician carbonate reservoirs in the Shunbei area: Frontiers in Earth Science, **10**, 1035735, doi: 10.3389/feart.2022.1035735.

Wei, J., L.-Y. Fu, Z. W. Wang, J. Ba, and J. M. Carcione, 2020, Green's function of the Lord-Shulman thermoporoelasticity theory: Geophysical Journal International, **221**, 1765–1776, doi: 10.1093/gji/ggaa100.

Xu, F., K. A. Seffen, and T. J. Lu, 2008, Non-Fourier analysis of skin biothermomechanics: International Journal of Heat and Mass Transfer, **51**, 2237–2259, doi: 10.1016/j.ijheatmasstransfer.2007.10.024.

Yang, J., L.-Y. Fu, T. C. Han, W. B. Deng, and B. Y. Fu, 2025, Thermoacoustoelasticity for elastic wave propagation in preheated and prestressed solid rocks: Rock Mechanics and Rock Engineering, **58**, 5143–5165, doi: 10.1007/s00603-024-04361-z.

Youssef, H. M., 2006, Theory of two-temperature-generalized thermoelasticity: IMA Journal of Applied Mathematics, **71**, 383–390, doi: 10.1093/imamat/hxh101.

Youssef, H. M., 2007, Theory of generalized porothermoelasticity: International Journal of Rock Mechanics and Mining Sciences, **44**, 222–227, doi: 10.1016/j.ijrmms.2006.07.001.

Yuan, H. M., D.-H. Han, L. X. Zhao, Q. Huang, and W. M. Zhang, 2019, Attenuation analysis of heavy oil sands based on laboratory measurements: Case history: Geophysics, **84**, no. 1, B299–B309, doi: 10.1190/geo2018-0171.1.

Zhang, Y., L.-Y. Fu, L. X. Zhang, W. Wei, and X. Z. Guan, 2014, Finite difference modeling of ultrasonic propagation (coda waves) in digital porous cores with un-split convolutional PML and rotated staggered grid: Journal of Applied Geophysics, **104**, 75–89, doi: 10.1016/j.jappgeo.2014.02.012.

Biographies and photographs of the authors are not available.